Piezocapacitive Flexible E-Skin Pressure Sensors Having Magnetically Grown Microstructures

Waqas Asghar, Fali Li, Youlin Zhou, Yuanzhao Wu, Zhe Yu, Shengbin Li, Daxiu Tang, Xintong Han, Jie Shang, Yiwei Liu,* and Run-Wei Li*

Flexible pressure sensors are highly desirable in artificial intelligence, health monitoring, and soft robotics. Microstructuring of dielectrics is the common strategy employed to improve the performance of capacitive type pressure sensors. Herein, a novel, low-cost, large-area compatible, and mold-free technique is reported in which magnetically grown microneedles are self-assembled from a film of curable magnetorheological fluid (CMRF) under the influence of a vertical curing magnetic field (B_{curing}). After optimizing the microneedles' fabrication parameters, i.e., magnetic particles' (MPs') concentration and B_{curing} intensity, piezocapacitive sensors capable of wide range pressure sensing (0–145 kPa) with ultrafast response time (50 ms), high cyclic stability (>9000 cycles), as well as very low detection limit (1.9 Pa) are obtained. Sensor properties are found dependent on microneedles' fabrication parameters that are controllable, produce variable-sized microneedles, and allow to govern sensing properties according to desired applications. Finally, the sensor is employed in holding a bottle with different weights, human breath, and motion monitoring, which demonstrate its great potential for the applications of human–machine interaction, human health monitoring, and intelligent soft robotics.

1. Introduction

Pressure-sensitive electronic skin (e-skin) has become important in the prosthetics, artificial intelligence, human–machine interaction, health monitoring, and soft robotics.[1–4] E-skin devices enable machines with tactile senses, e.g., "Co-robots," use e-skin to friendly interact with human beings, working environment

and other robots.[5] Especially communication of home service robots and artificial limbs with human beings is carried out via friendly human–machine interaction.[6] An ideal e-skin is expected to be highly flexible, sensitive, lightweight, easy to fabricate, inexpensive, and should be capable of performing like the natural skin, which feels tactile pressures ranging from light touches (0–10 kPa) to object handling levels (10–100 kPa).[2,6–12] Generally, e-skin pressure sensors use piezoresistive,[10,13,14] piezocapacitive,[8,15–17] piezoelectric,[2,18] and triboelectric[19] sensing mechanisms to transduce applied pressure into an electrical signal. Particularly, piezocapacitive pressure sensors are quite attractive due to their simple structure, fast response time, low power consumption, and compact circuit layout.[1,17]

A capacitive pressure sensor typically consists of two parallel electrodes that sandwich a polymeric dielectric layer. An external force applied to the capacitive sensor changes the thickness of its dielectric layer, which leads to the variation in its capacitance. The sensing performance of such a sensor is determined by mechanical properties of its elastomeric dielectric layer, i.e., greater the compressibility of the material used, the greater the sensitivity of the sensor will be.[20] Polydimethylsiloxane (PDMS) is considered a suitable candidate for pressure-sensitive dielectric thin films,[9] but its high Young's modulus (≈2 MPa)[21]

W. Asghar, F. Li, Y. Zhou, Y. Wu, Z. Yu, S. Li, D. Tang, X. Han,
Prof. J. Shang, Prof. Y. W. Liu, Prof. R.-W. Li
CAS Key Laboratory of Magnetic Materials and Devices
Ningbo Institute of Materials Technology and Engineering
Chinese Academy of Sciences
Ningbo 315201, P. R. China
E-mail: liuyw@nimte.ac.cn; runweili@nimte.ac.cn
W. Asghar, F. Li, Y. Zhou, Y. Wu, Z. Yu, S. Li, D. Tang, X. Han,
Prof. J. Shang, Prof. Y. W. Liu, Prof. R.-W. Li
Zhejiang Province Key Laboratory of Magnetic Materials
and Application Technology
Ningbo Institute of Materials Technology and Engineering
Chinese Academy of Sciences
Ningbo 315201, P. R. China

The ORCID identification number(s) for the author(s) of this article can be found under https://doi.org/10.1002/admt.201900934.

W. Asghar
International School
University of Chinese Academy of Sciences
Beijing 100049, P. R. China
W. Asghar
Mechanical Engineering Department
University of Engineering and Technology Taxila
47050 Taxila, Pakistan
F. Li, Y. Wu, Z. Yu, D. Tang, X. Han, Prof. R.-W. Li
College of Materials Science and Opto-Electronic Technology
University of Chinese Academy of Sciences
Beijing 100049, P. R. China
S. Li, Prof. R.-W. Li
School of Future Technology
University of Chinese Academy of Sciences
Beijing 100049, P. R. China

**ADVANCED
SCIENCE NEWS**
www.advancedsciencenews.com

**ADVANCED
MATERIALS
TECHNOLOGIES**
www.advmattechnol.de

makes it less deformable, toward minute applied pressures (e.g., <1 kPa).[22] Besides this, only a few micrometer (µm) thick flat PDMS dielectric films exhibit significant viscoelastic creep, which leads to lesser compressibility and increased relaxation times after removal of pressure.[8,9,20] To cope with these problems, thin dielectric films are microstructured by using geometries like domes,[23,24] pyramids,[14,25,26] and pillars.[27–29] This microstructuring provides voids that enable the microstructured surfaces to deform elastically on the application of external pressure, thereby storing and releasing the energy reversibly and thus improves the overall sensor's performance and minimizes the problems associated with viscoelastic behavior.[9]

Manufacturing of microstructured dielectric films often require molds, which are produced either from certain natural materials or from complicated photolithography and chemical etching processes.[9,10,22,30] Natural-material-based molds produce microstructures of specific dimensions while other processes involve multisteps: casting, degassing, vacuum annealing, and peeling of PDMS film, which are not ideal for low cost and large-area manufacturing.[30] Moreover, some indispensable materials and devices such as Si mold, photoresist, shadow mask, nanowires, Eco-flex, and polymer gel increase the overall manufacturing cost and time.[31] By using the above-mentioned processes, previously reported microstructured sensors are generally fabricated, by keeping the research focus on detecting weak pressure signals, which limits the detection range of pressure sensors in the low-pressure regime.[22,32] This implies that a simple and more reliable method should be developed that allows easy tailoring of the microstructures to achieve required pressure sensing performance in the desired detection range.

Herein, we present a novel, low-cost, mold-free, and large area-compatible technique to fabricate flexible pressure sensors by using magnetically grown dielectric interface (MGDI). The 3D microneedles are directly self-assembled, by spin coating a film of curable magnetorheological fluid on the bottom electrode, followed by moving the electrode to vertical B_{curing}. Manufacturing parameters like magnetic particles' (MPs') concentrations and B_{curing} are varied to obtain good performance sensor, followed by exploring the effect of these parameters on needles' aspect ratio, density, and Young's modulus, and finally correlating them with the sensors' sensing performance. This technique allows the large scale production of pressure sensors in a fast, easy, low-cost and mold-free way with great freedom to attain tunable sensing performance in desired pressure range, by simply controlling the sensor's manufacturing parameters, thus being a robust alternative to the generic approaches for the films microstructuration. The performance of our sensors is comparable to previously reported sensors and high benefit/cost ratio of our technique makes it a wise choice for the applications of motion detection, health monitoring, human–machine interaction, and soft robotics.

2. Results and Discussion

2.1. Preparation of Flexible Pressure Sensor

Figure 1a shows the fabrication process and device structure of a flexible capacitive pressure sensor. The process starts by spin coating a layer of PDMS on a glass slide followed by applying liquid metal (LM) paste. Afterward, another PDMS layer is spin-coated, which completes the formation of top electrode. Bottom electrode manufacturing is also similar to that of top electrode, except including an additional step of spin coating a layer of curable magnetorheological fluid (CMRF) on it. CMRF consists of silver-coated nickel (Ag@Ni) MPs uniformly mixed in PDMS. After the spin-coating of CMRF, bottom electrode is slowly moved into the external B_{curing}, which magnetized the MPs, particles started aggregating in chains, divided into small peak and valley patterns and ultimately results in the formation of tilted liquid microneedles.[33–36] Inset of Figure 1a describes the formation of microneedles by varying the intensity and angle of B_{curing}. Liquid microneedles are distributed along magnetic field direction and gradually rotate with the change in the direction of external B_{curing}. Finally, vertical microneedles are attained by moving bottom electrode to the central region of two magnets—where magnetic field direction is perpendicular to the electrode. Formation of such microneedle-based patterns under vertical magnetic field is called normal-field or the Rosensweig instability.[33,35] Liquid microneedles maintain their vertical position under the combined effect of gravity, surface tension, and magnetic force.[33] Higher B_{curing} results in the formation of large size, less dense needles, and vice versa (inset of Figure 1a).

The self-assembled liquid microneedles (under the external magnetic field) are heated and then solidified owing to the polymerization reaction of PDMS. After curing and peeling of bottom electrode, the flexible pressure sensor is obtained by laminating the top electrode on micropatterned bottom electrode. Figure 1b–d shows scanning electron microscope (SEM) images of magnetically induced microneedles in different views. Length, width, and density of needles depend upon B_{curing} intensity and concentration of MPs mixed in PDMS, which will be discussed later. By following above manufacturing steps, we obtained 16 different test samples, based on various MPs: PDMS w/w ratios (1:1, 1.5:1, 2:1, 2.5:1) and B_{curing} intensities (135, 148, 156, 170 mT).

2.2. Electromechanical Characterization of Piezocapacitive Sensors

The sensing performance of the flexible capacitive pressure sensor is evaluated in **Figure 2**. The sensitivity of a capacitive sensor is given by

$$\frac{\delta\left(\dfrac{\Delta C}{C_0}\right)}{\delta P} \tag{1}$$

where C_0 represents initial capacitance, ΔC corresponds to capacitance change ($C - C_0$), and P is the compressive pressure applied.[11] Figure S1 (Supporting Information) shows the relative change in capacitance of samples, in the range of 0–145 kPa. Sensors' sensitivity is calculated by measuring the slope of tangent, drawn on sensors' $\Delta C/C$ versus P curves. Sensors have shown three distinct pressure ranges characterized by different sensitivities. These pressure ranges may be defined as low-pressure regime (0–1 kPa), medium pressure regime (1.5–11 kPa), and the high-pressure regime (12–145 kPa).
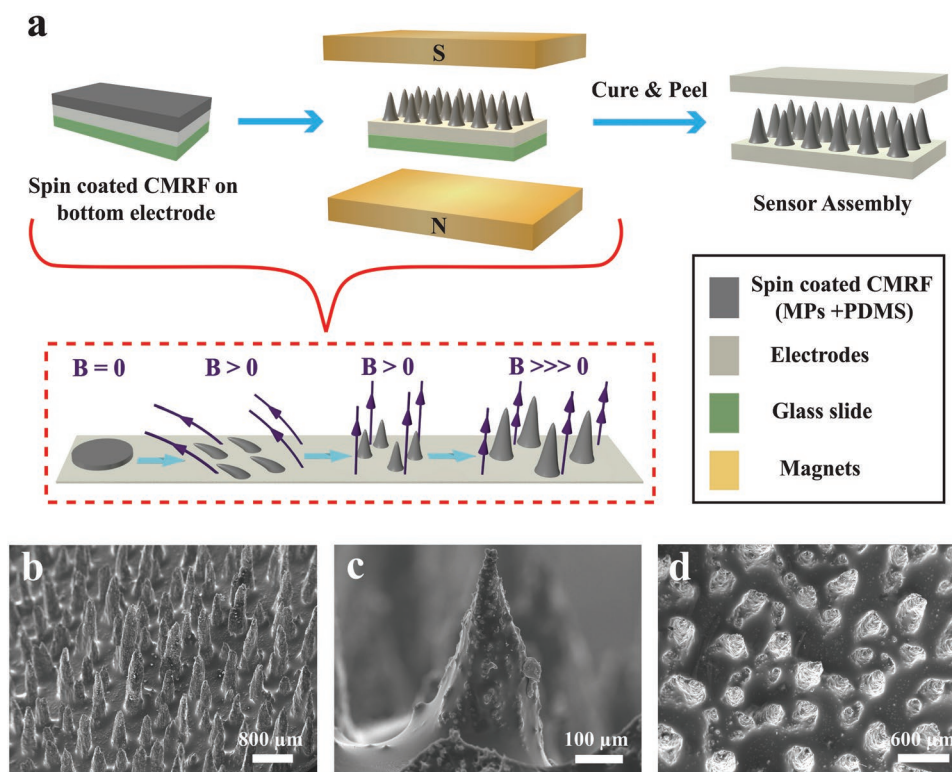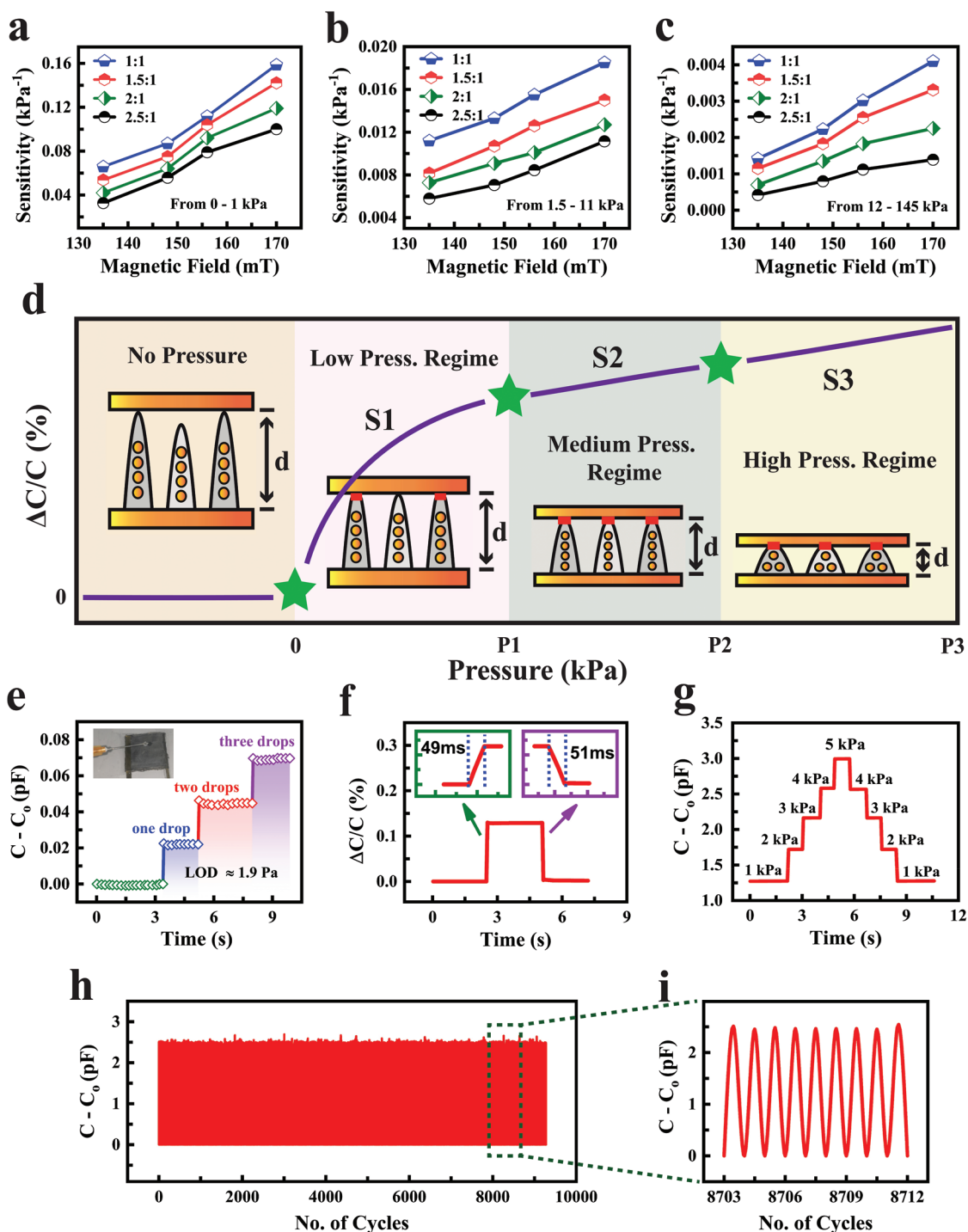
Figure 1. Fabrication of capacitive type flexible pressure sensor. a) Schematic illustration for the fabrication of MGDI-incorporated pressure sensor. The inset figure shows the MGDI formation by changing magnitude and direction (angle) of B_{curing}, higher magnetic field results in large size, less dense needles, and vice versa. Final sensor assembly consists of top electrode/MGDI/bottom electrode. SEM images of MGDI layers captured in views: b) 45° tilted view, c) side view, and d) top view.

Figure 2a–c shows the sensors' sensitivities in low, medium and high-pressure regimes. It is evident from graphs that MPs' concentration in PDMS exhibits inverse relation with the sensitivity of sensors. Sensitivity decreases with the increase of MPs' concentration, which might be caused because of the hardening of microneedles. Out of all concentrations, 1:1 w/w ratio is found ideal for achieving better sensing performance in all the pressure regimes. Conversely, sensitivity increases with the increase of B_{curing} from 135 to 170 mT. Curing magnetic field is found more effective to influence the sensor performance than increasing MPs' concentration. To further elaborate the impact of B_{curing}, we simplify the discussion by taking 1:1 sample as a reference. When the sensitivity of 1:1 sample cured at 135 and 170 mT is compared, the sample has shown a percentage increase of 141%, 65.35%, and 188.732% in low, medium, and high-pressure regimes, respectively.

The sensitivity of all samples decreases with the increase of pressure, and this trend is quite similar to that of previously reported flexible pressure sensors.[32,37,38] Sensor 1:1 @ 170 mT has shown maximum overall performance with sensitivities of 0.159, 0.019, and 0.0041 kPa^{-1} in low, medium, and high-pressure regimes. Figure S2 (Supporting Information) compares the sensitivity of the microstructured sensor (1:1@170 mT) and non-microstructured sensor (having same dimensions as microstructured sensor). The non-microstructured sensor exhibits sensitivity of 0.0003 kPa^{-1} in high-pressure regime, which is identical to previously reported work[22] and is 91.46% lower than the sensitivity of 1:1 @170 mT sensor, within

same pressure regime. Generally, microstructured pressure sensors manufactured by complex and expensive methods are only suitable for short pressure ranges. Working range of most of the reported sensors lies ≤10 kPa,[9,39–43] some work up to 20 kPa[8,20,44,45] and only few reaches up to ≤50 kPa pressure range.[17,46] Also, their output saturates when applied pressure exceeds some critical value. By contrast, our sensor (1:1 @170 mT) responds linearly to applied pressure, even at very high pressure up to 145 kPa. Such a wide range pressure sensing response shows that the use of a low-cost technique with lower precision than photolithography techniques does not impair the sensor performance.

Figure 2d shows the possible explanation of three different sensitives in terms of change of microneedles' geometries. In low-pressure regime, sensors' have shown maximum sensitivity (characterized by a sensitivity of S1), which may be attributed to the presence of minute airgap and touching of some larger size needles to the inner surface of the upper electrode, as shown in Figure 2d (low-pressure regime). In the medium pressure regime, remaining short sized needles also begin to touch with the electrode in addition to squeezing of large size needles, as shown in Figure 2d (medium pressure regime). This leads to an increase in overall contact area, as more needles get contacted with the electrode and the contact area of each microneedles also increases that's why sensitivity in this regime, S2, is smaller than S1. During compression, conical structures bear nonuniform stress distribution, in which stress is wholly concentrated at their pointed tips rather than the

**ADVANCED
SCIENCE NEWS**

www.advancedsciencenews.com

**ADVANCED
MATERIALS
TECHNOLOGIES**

www.advmattechnol.de

Figure 2. Electromechanical characterization of piezocapacitive pressure sensors. Sensitivity variation of sensors obtained in the pressure range of: a) 0–1 kPa, b) 1.5–11 kPa, and c) 12–145 kPa. MGDI of sensors is manufactured at various MPs: PDMS w/w ratios and different B_{curing} intensities. d) Capacitance change mechanism of microstructured sensor w.r.t. applied pressure. e) LOD of the sensor determined through the dispensation of a water drop (≈1.9 Pa). f) Response time of the sensor, calculated at 2.5 kPa. The insets show the response time upon loading and unloading. g) Capacitance signals at repeated pressures of 1, 2, 3, 4, and 5 kPa, indicating good repeatability of the sensor. h) Stability of the sensor tested for ≈ 9200 cycles under an applied pressure of 4 kPa. i) Detailed capacitance signals from 8703 to 8712 cycles.

broader base. Thus, the tip of conical structures compresses more due to its smaller area which results in higher mechanical deformation at the top.[8,20] Therefore, conical structures

show large sensitivity initially due to small contact area, which drops at higher compressive pressures with the increase of contact area, and structure itself reverts to a more truncated

**ADVANCED
SCIENCE NEWS**

www.advancedsciencenews.com

**ADVANCED
MATERIALS
TECHNOLOGIES**

www.advmattechnol.de

cross-sectional area.[6,9,20] In high-pressure regime, cones are fully compressed, increase of applied pressure only contributes to a very small change in contact area, which transduces minute change in capacitance, with a sensitivity of S3, smaller than S2. Also, high compression may slightly change the fixed position of MPs in microneedles.

Further tests conducted on the sensor are reported herein. To determine the limit of detection (LOD), a water drop of $\approx(13 \pm 2)$ mg was dispensed on the top of sensor, exerting a pressure of (1.9 ± 0.2) Pa, as shown in Figure 2e. Successful detection of such a minute pressure confirms that our device exhibits ultralow LOD, which equals or surpasses the LOD of previously reported microstructured sensors, varying from 0.5–17.5 Pa.[6,8,9,16,28,31,38,44,47–49] To determine the sensor's response time, we applied 2.5 kPa pressure on sensor by using Instron (2400 mm min^{-1}). The sensor presents a response time of (50 ± 1) ms, which is comparable to the response time of human skin (30–50 ms) and that of other reported microstructured sensors, prepared through photolithography or natural molds.[6,8,15,48,50,51]

Furthermore, we investigated the sensor's repeatability by applying pressures of 1, 2, 3, 4, and 5 kPa on it, and results confirm that our sensor exhibits stable response with high repeatability (Figure 2g). In addition, our sensor endured $\approx$9200 loading–unloading cycles at $\approx$4 kPa (rate = 99 mm min^{-1}) and maintained its function with minimal output signal degradation (Figure 2h), confirming that it is a highly robust MGDI-incorporated pressure sensor. Figure 2h shows that the capacitance signal keeps its amplitude and waveform at different stages of test, confirming the high stability of the device. The good performance of our sensor in terms of response time, LOD and mechanical robustness associated with its wide range sensing capability, reinforces the fact that current manufacturing technique, which makes a compromise between precision, low-cost, and speed, is suitable to produce efficient piezocapacitive sensors with high benefit/cost ratio. In addition, design and performance tailoring capability of this technique makes it unique to optimize sensors' performance in much wider pressure range by fast and easy way of just controlling manufacturing parameters (MPs' concentration and B_{curing}).

2.3. Characterization of Microneedles

The performance of our sensor is highly dependent on MGDI, which consists of microneedles manufactured by varying MPs: PDMS w/w ratios and B_{curing} intensities. We have calculated various parameters: aspect ratio, density and Young's modulus of needles to investigate the effect of these parameters on the sensing performance. These parameters and their
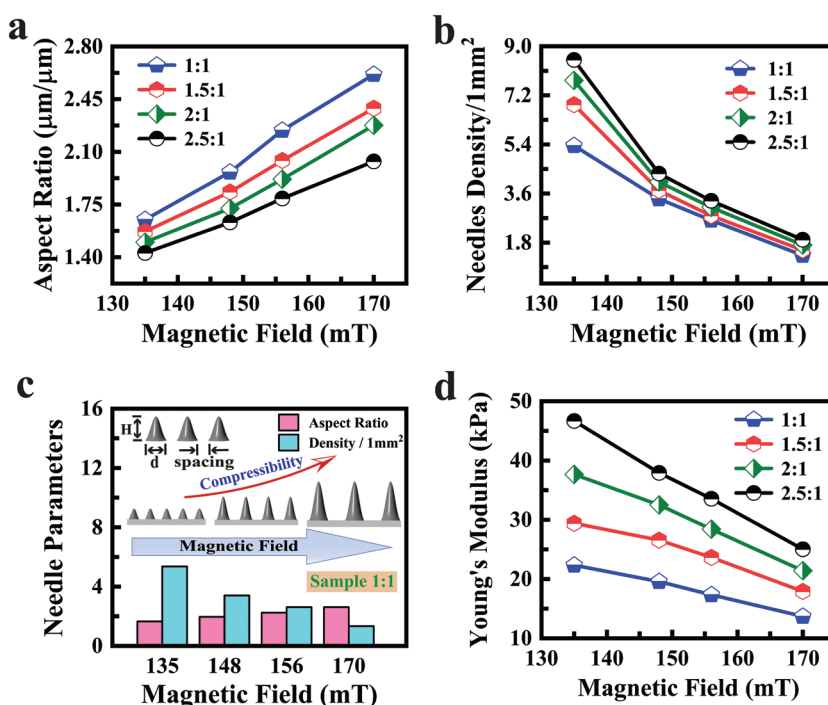
Figure 3. Parameters' evaluation of microneedles. a) Aspect ratio (height/diameter) variation of microneedles. Height and diameter of microneedles are obtained from their SEM pictures shown in Supporting Information. b) Variation of needles density w.r.t. curing magnetic field and MPs: PDMS w/w ratios. c) Bar graph showing aspect ratio and density variation of 1:1 samples with increasing B_{curing}. The inset figure shows that an increasing magnetic field simultaneously affects needle's height, diameter, spacing, and density. d) Young's modulus (E) variation w.r.t. curing magnetic field values and MPs: PDMS w/w ratios. Young's modulus is calculated from stress–strain curves of needles shown in the Supporting Information.

correlation with sensing performance are discussed herein. Figure S3 (Supporting Information) shows the SEM images of microneedles. These images are used to calculate the height and diameter of microneedles, as illustrated in Figure S4 (Supporting Information). Needles' height is measured from their tip to their base, and their diameter corresponds to the base width of each microneedle measured in horizontal direction. We have obtained needles' height and diameter in the range of 275–856 μm and 166–420 μm, respectively. Both height and diameter of needles increases with the increase of B_{curing} intensity and MPs' concentration. However, B_{curing} affects the needles' dimensions more effectively than MPs' concentration (Figure S4a,b, Supporting Information). **Figure 3**a shows the variation of aspect ratio (height/diameter) of microneedles. Microneedles' aspect ratio lies in the range of 1.42–2.61, bearing the same increasing trend as that of needles' height and diameter. Microneedles of 1:1 sample (minimum MPs' concentration) exhibit maximum aspect ratio out of all, with a percentage increase of 58.18%, when B_{curing} is increased from 135 to 170 mT. It is to be worth mentioning that other researchers have previously attained aspect ratio 0.5–2 by using complex and expensive techniques but we have attained a much larger aspect ratio of 2.61, in a very cost-effective way.[8–10]

Figure S5 (Supporting Information) shows the microscopic images of microneedles. These images are used to calculate the density mm^{-2} of microneedles, shown in Figure 3b. Needles'

**ADVANCED
SCIENCE NEWS**

www.advancedsciencenews.com

**ADVANCED
MATERIALS
TECHNOLOGIES**

www.advmattechnol.de

density is found directly proportional to MPs' concentration and inversely related to B_{curing}. Higher curing magnetic field intensity results in less dense needles that are spaced farthest apart. Figure S4c (Supporting Information) shows that interneedle spacing increases with the increase of B_{curing}. Sample 1:1 @ 170 mT exhibits least dense needles (1.33 needles mm^{-2}) with maximum interneedle spacing, i.e., 604 µm.

There exists a correlation between the above-mentioned needle parameters and the magnitude of B_{curing}, which can be explained in terms of magnetic chains formation. Magnetic chains formed under an external magnetic field are the backbone of liquid microneedles. During the formation of liquid microneedles, these chains act as magnetic dipoles which attract each other and grow bigger. Magnetized particles present in these chains, support this aggregation. The bigger aggregation attracts more and more magnetic particles around it and the process becomes faster at higher magnetic fields.[33,34,52,53] So, liquid microneedle containing a relatively large number of MPs attracts nearby small-sized needles, which collapse and start aggregating with this needle. This phenomenon reduces needles' density and simultaneously increases the height, diameter, and interneedle spacing of needles. Since 1:1 sample has shown superior performance in terms of aspect ratio and density, so we have presented its parameters in the form of bar graph (Figure 3c) for clear understanding. The inset figure shows that increasing the intensity of B_{curing}, reduces needles density and simultaneously enhances the height, diameter, and spacing of needles.

Effect of manufacturing parameters on the elasticity of microneedles is analyzed by conducting compression tests on microneedles (Figure S6, Supporting Information), followed by calculating Young's modulus (E) from the slope of linear elastic region of needles' stress–strain curves.[54] Compression tests are performed at a strain rate of 0.5 mm min^{-1} by using Instron machine. Figure 3d shows the experimentally obtained values of Young's modulus. It is evident that increasing MPs' concentration also increases Young's modulus and reduces the elasticity of microneedles.[33] Microneedles of 1:1 sample exhibit least E, which is required for high performance of sensor. More interestingly, E also decreases with increasing B_{curing} values. Microneedles of 1:1 sample have shown 38.67% decrease in Young's modulus when B_{curing} increases from 135 to 170 mT. This can be explained in terms of aspect ratio and density of needles. At higher B_{curing}, less dense and high aspect ratio microneedles are formed. Microneedles with higher aspect ratio are easier to destabilize and have more room to be compressed. If the density of such needles is also reduced, their interneedle spacing increases, which makes the dielectric layer even more "softer," and thus improves the sensitivity.[8]

Sample 1:1@170 mT exhibits least Young's modulus, i.e., 13.7 kPa, with an average interneedle spacing of ≈604 µm. High aspect ratio and less dense needles with least Young's modulus are the factors that are responsible for the superior performance of 1:1@170 mT, out of all. And samples with least aspect ratio and inter needle-spacing have shown least sensitivity, due to their least sensitivity to mechanical compression.[20] Sensors having microneedles spaced farthest apart are found more sensitive to mechanical compression. Bao and co-workers have reported a microstructured pressure sensor, in which they used

photolithography to prepare pure PDMS-based micropyramids and finally attained $E \approx 10.9$ kPa with the spacing of 100 µm.[20] Although, we have attained larger spacing and aspect ratio as compared to their work, but still E of our sample 1:1 @ 170 mT is slightly higher than that presented by Bao et al., which is attributed to the presence of MPs inside.

2.4. Application Demo

To demonstrate the practical application of our sensor, we monitored the capacitance change arising from variety of pressure sources, which are illustrated in **Figure 4**. The real-time response of our sensor generated by holding a bottle is shown in Figure 4a in which the amplitude of capacitance signal increases with the increase of weight of the object. The sensor was attached to the thumb and the weight of bottle was increased by adding coca cola inside it. During holding, bottle sliding was judged by a finger and gripping force was increased simultaneously from thumb to avoid slipping of the bottle. In robotics, this can be attained by using another shear sensor at the same time to get exact information about increasing the force and to avoid slipping of an object. Sensor response confirms that it is highly capable of monitoring pressure signals arising from different pressure sources and can be used successfully in industrial robots, especially in the area of automated storage and retrieval systems (automatically picking and placing loads from defined storage locations).

Figure 4b shows the real-time response of our sensor to human breathing. This response is monitored by using a smart mask, which consists of a sensor attached inside it. The sensor has shown remarkable peaks to pressure signals arising from normal breathing, fast breathing by nose and fast breathing orally. The normal breathing rate of human body is between 12–18 breaths min^{-1},[55] which efficiently allows for adequate amounts of oxygen to get into the lungs and carbon dioxide to leave. The balance of these gases in the human body is disturbed by various disorders leading to hyperventilation or hypoventilation. Hyperventilation is fast breathing, in which a person breathes deeper than normal.[56] Patients of panic disorder, asthma, anemia and anxiety face hyperventilation,[57] so by using this mask one can easily monitor their breathing at home. The increased breathing rate of a person during hiking can also be monitored easily at high altitudes, by using our mask. Hypoventilation is another breathing phenomenon, which is characterized by slow and ineffective breathing.[58] This disorder occurs due to various factors: drug overdosage, using antidepression or antianxiety drugs, or drinking excess alcohol.[55] Obese people also suffer hypoventilation during their sleep time.[59] So, the breathing rate of hypo-ventilated persons can be monitored effectively during their daily life activities, by using our smart mask. Besides, this mask is also useful for the patients suffering from antrochoanal and pregnancy rhinitis, who breathe only orally due to some nasal obstruction, which prevents normal breathing through nose.[60]

Moreover, we tested the sensor's dynamic sensing capability by placing a small live turtle (91 g) onto the pressure sensor. When turtle started moving on the sensor, the capacitance of sensor changed according to the moving actions of
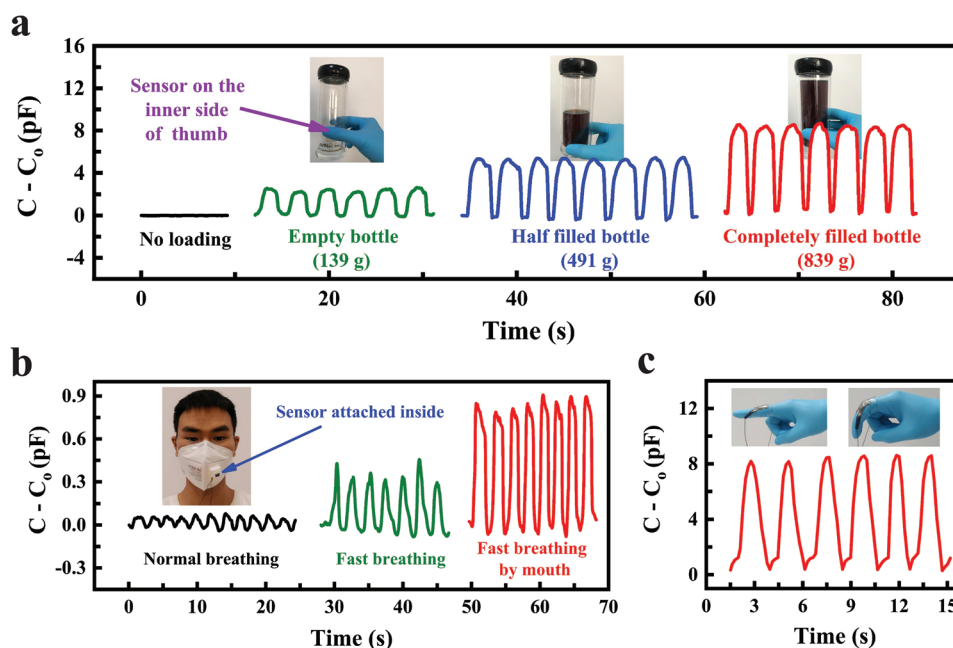
Figure 4. Applications of the MGDI-incorporated flexible pressure sensor (1:1 @ 170 mT). Real-time monitoring of capacitance variations arising from a variety of pressure sources, such as: a) holding bottle with different amounts of liquid inside it, b) different stages of human breathing, and c) finger bending.

the turtle (as illustrated in Figure S7a, Supporting Information). Such type of dynamic interaction is highly required in artificial intelligence, service robots, and artificial limbs.[3,5] The simple response of the sensor to normal pressing is shown in Figure S7b (Supporting Information), in which sensor successfully detects the repeated finger touching, which confirms its high capability to "feel" human touch. Besides, our sensor also monitored the various repeated flexion and straightening motions of the finger, and wrist while exhibiting reproducible response (Figure 4c and Figure S7c, Supporting Information), demonstrating its potential to be applied in the field of human motion inspection (monitoring) and even artificial intelligence. Furthermore, when performance of our sensor is tested under external magnetic field ($B_{ext.}$), its performance is found to be sensitive to $B_{ext.}$ (as illustrated in Figure S8a,b, Supporting Information), which can be attributed to $B_{ext.}$ interaction with the MPs present inside each microneedle. Our sensor exhibits an interesting simultaneous response to pressure and magnetic signals which can be used for tactile and touchless interaction in future bi-functional e-skins. For example, Jin et al.[61] have combined two sensors–pressure and giant magneto resistance sensor, to sense pressure and magnetic signals simultaneously. However, our sensor is exhibiting superior performance in a sense that without combining any additional sensor, our sensor efficiently responds to pressure and magnetic signals at the same time.

3. Conclusion

In this work, we presented a novel, low-cost, large-area compatible, and mold-free technique that utilizes magnetically microstructured dielectric films to fabricate flexible pressure sensors. After design optimization, sensor having interface

prepared at 1:1 @ 170 mT (lowest MPs' concentration and highest B_{curing}) has shown optimized sensing properties in wide pressure sensing range (0–145 kPa) with ultrafast response time (50 ms), high robustness (>9000 cycles), as well as very low detection limit (1.9 Pa). Parameter's evaluation of dielectric microneedles indicates that sample 1:1 @ 170 mT exhibits high aspect ratio (2.61) and less dense microneedles (1.33 mm^{-2}) with least Young's modulus (13.7 kPa), which results in its optimized sensing properties. Our sensor has shown adequate performance during the holding of different weight object, human breath monitoring, touch sensing, and motion monitoring, which confirm its great potential for various applications such as robotics, human–machine interfaces, artificial intelligence, and real-time human health monitoring systems.

Furthermore, the current fabrication process is proved highly proficient to produce high-performance pressure sensors on large scale with high benefit/cost ratio by just controlling the manufacturing parameters (MPs' concentration and B_{curing}). However, by using electromagnet instead of permanent magnet, higher B_{curing} intensities can be achieved very easily, which will produce microneedles of more higher aspect ratio with lesser densities, and large-scale production will be realized more easily.

4. Experimental Section

Chemicals and Materials: PDMS (Sylgard 184, Dow Corning, USA) and silver coated nickel (Ag@Ni) MPs (average diameter: ≈ 14 µm, Potters Industries Inc., USA) were purchased from the market. High-purity metals gallium, indium, and tin (99.99%, Beijing Founde Star Sci. & Technol. Co., Ltd) were mixed in the ratio of 68.2:21.8:10 by mass. Then the above mixture was heated and stirred at 60 °C for 30 min to obtain LM Galinstan ($Ga_{68.2} In_{21.8} Sn_{10}$). LM paste was prepared by mixing Cu

ADVANCED
SCIENCE NEWS

www.advancedsciencenews.com

ADVANCED
MATERIALS
TECHNOLOGIES

www.advmattechnol.de

particles (average diameter: ≈ 1 µm, ZhongNuo Advanced Material Technology Co., Ltd., China) in laboratory-prepared Galinstan in a ratio of 20% (w/w).

Preparation of Flexible Electrodes: PDMS was prepared in a 10:1 w/w ratio (base to curing agent) and then degassed to remove air bubbles. A piece of glass slide (250 mm × 250 mm) was taken, and it was sprayed with mold release agent (Ease Release-200, Mann Release Technologies Inc., USA) prior to spin coating, which assisted in peeling of cured samples at the end. Then PDMS mixture was spin-coated at 600 rpm on glass slide, followed by curing in an electric oven at 80 °C for 35 min. After curing, a copper strip (0.3 mm thick and 3 mm wide) was attached to this PDMS layer by using flexible glue (Shenzhen Yuanxunda Chemical Technology Co., Ltd., China), which finally served as electrode. Then LM layer was applied on PDMS layer by ensuring the good electrical contact between Cu strip and LM paste. Afterward, another PDMS layer was spin-coated at 600 RPM, followed by curing it in electric oven at 80 °C for 35 min. This curing completes the fabrication of flexible electrodes. LM metal paste hinders the formation of strong bond between first and second PDMS layers, so 3 mm LM paste was removed from all edges of sample prior to the deposition of second spin-coated PDMS layer.

Preparation of CMRF, MGDI, and Pressure Sensors: CMRF was prepared by uniform mixing MPs of silver-coated nickel (Ag@Ni) and PDMS in 1:1, 1.5:1, 2:1, 2.5:1 w/w ratios (MPs to PDMS). Finally, MGDI-incorporated bottom electrodes were prepared by spin coating CMRF layer (600 rpm) on some of the previously prepared flexible electrodes, followed by placing the samples between parallel placed permanent magnets (Dongguan Yanghua Magnet Factory, China). For this purpose, an acrylic mold having aluminum nuts and bolts was developed. Magnets were placed in the mold in face to face parallel form and mold's height remained adjustable due to the provided nuts and bolts. Vertically aligned needles were attained, by moving the CMRF-deposited sample, from edge to center of magnets (needles' angle changed with the change of angle of magnetic field). B_{curing} intensity along the *z*-direction was tuned by adjusting the distance between two magnets or by changing the position of sample in the *z*-direction, which was placed between two magnets in mold. Vertically aligned liquid microneedles were cured at 80 °C for 1 h by placing the mold containing bottom electrode and magnets in an electric oven under vacuum. After solidification, the bottom electrode was peeled off and top electrode was placed on it. Finally, PDMS strips (250 mm × 4 mm × 0.8 mm) were placed at device edges and then edges were sealed with flexible glue. The final size of each sensor was 250 mm × 250 mm × 1.5 mm.

Characterization and Measurements: Morphological characterization of microneedles was done by using SEM (EVO 18, ZEISS, Germany) and digital microscope (SteREO Discovery V12, ZEISS, Germany) images were used to calculate the density of microneedles. Magnetic field intensity of permanent magnets was measured by using Gauss meter (PF-035, Li-Tian Magnetoelectrican Science &Technology Co., Ltd., China). Electromechanical and Young's modulus evaluation tests were carried out by using a computer-controlled material testing machine (Instron 5943, USA). Pressure was applied at the center of the sensor by using a plastic rod of 5.88 mm dia. Sensors' capacitance variations were measured by using LCR meter (IM 3570, HIOKI, Japan) with a test frequency of 400 kHz. During pressure-dependent capacitance measurements, a thick wooden block was placed beneath each sensor to avoid any metal interference during testing. The capacitance signals during application demo were measured by using the same LCR meter, without using any additional amplification component. The impact of external magnetic field on the performance of sensor was evaluated by placing the sensor on permanent magnet and the resulting magnetic field intensity was varied by placing various wooden blocks beneath the sensor. Pressure was applied by using Instron machine and resulting capacitance variations were measured by using LCR meter.

Ethical Statement: Informed signed consent was obtained from the human subject to conduct all the experiments reported in this manuscript.

Supporting Information

Supporting Information is available from the Wiley Online Library or from the author.

Conflict of Interest

The authors declare no conflict of interest.

[1] X. Wang, L. Dong, H. Zhang, R. Yu, C. Pan, Z. L. Wang, *Adv. Sci.* **2015**, *2*, 1500169.

[2] Y. Zang, F. Zhang, C.-a. Di, D. Zhu, *Mater. Horiz.* **2015**, *2*, 140.

[3] T. Yang, D. Xie, Z. Li, H. Zhu, *Mater. Sci. Eng., R* **2017**, *115*, 1.

[4] Y. Wan, Y. Wang, C. F. Guo, *Mater. Today Phys.* **2017**, *1*, 61.

[5] H. Ding, X. Yang, N. Zheng, M. Li, Y. Lai, H. Wu, *Natl. Sci. Rev.* **2018**, *5*, 799.

[6] Z. Qiu, Y. Wan, W. Zhou, J. Yang, J. Yang, J. Huang, J. Zhang, Q. Liu, S. Huang, N. Bai, Z. Wu, W. Hong, H. Wang, C. F. Guo, *Adv. Funct. Mater.* **2018**, *28*, 1802343.

[7] L. Wang, D. Chen, K. Jiang, G. Shen, *Chem. Soc. Rev.* **2017**, *46*, 6764.

[8] Y. Wan, Z. Qiu, Y. Hong, Y. Wang, J. Zhang, Q. Liu, Z. Wu, C. F. Guo, *Adv. Electron. Mater.* **2018**, *4*, 1700586.

[9] S. C. Mannsfeld, B. C. Tee, R. M. Stoltenberg, C. V. H. Chen, S. Barman, B. V. Muir, A. N. Sokolov, C. Reese, Z. Bao, *Nat. Mater.* **2010**, *9*, 859.

[10] A. dos Santos, N. Pinela, P. Alves, R. Santos, E. Fortunato, R. Martins, H. Águas, R. Igreja, *Adv. Electron. Mater.* **2018**, *4*, 1800182.

[11] Y. Wan, Z. Qiu, J. Huang, J. Yang, Q. Wang, P. Lu, J. Yang, J. Zhang, S. Huang, Z. Wu, C. F. Guo, *Small* **2018**, *14*, 1801657.

[12] Y. Wu, Y. Liu, Y. Zhou, Q. Man, C. Hu, W. Asghar, F. Li, Z. Yu, J. Shang, G. Liu, R.-W. Li, *Sci. Rob.* **2018**, *3*, eaat0429.

[13] H. Tian, Y. Shu, X.-F. Wang, M. A. Mohammad, Z. Bie, Q.-Y. Xie, C. Li, W.-T. Mi, Y. Yang, T.-L. Ren, *Sci. Rep.* **2015**, *5*, 8603.

[14] C. L. Choong, M. B. Shim, B. S. Lee, S. Jeon, D. S. Ko, T. H. Kang, J. Bae, S. H. Lee, K. E. Byun, J. Im, Y. J. Jeong, C. Park, J.-J. Park, U.-I. Chung, *Adv. Mater.* **2014**, *26*, 3451.

**ADVANCED
SCIENCE NEWS**

www.advancedsciencenews.com

**ADVANCED
MATERIALS
TECHNOLOGIES**

www.advmattechnol.de

[15] S. Kang, J. Lee, S. Lee, S. Kim, J. K. Kim, H. Algadi, S. Al-Sayari, D. E. Kim, D. Kim, T. Lee, *Adv. Electron. Mater.* **2016**, *2*, 1600356.

[16] T. Li, H. Luo, L. Qin, X. Wang, Z. Xiong, H. Ding, Y. Gu, Z. Liu, T. Zhang, *Small* **2016**, *12*, 5042.

[17] S. H. Cho, S. W. Lee, S. Yu, H. Kim, S. Chang, D. Kang, I. Hwang, H. S. Kang, B. Jeong, E. H. Kim, S. M. Cho, K. L. Kim, H. Lee, W. Shim, C. Park, *ACS Appl. Mater. Interfaces* **2017**, *9*, 10128.

[18] C. Dagdeviren, Y. Su, P. Joe, R. Yona, Y. Liu, Y.-S. Kim, Y. Huang, A. R. Damadoran, J. Xia, L. W. Martin, Y. Huang, J. A. Rogers, *Nat. Commun.* **2014**, *5*, 4496.

[19] L. Lin, Y. Xie, S. Wang, W. Wu, S. Niu, X. Wen, Z. L. Wang, *ACS Nano* **2013**, *7*, 8266.

[20] B. C. K. Tee, A. Chortos, R. R. Dunn, G. Schwartz, E. Eason, Z. Bao, *Adv. Funct. Mater.* **2014**, *24*, 5427.

[21] F. Schneider, T. Fellner, J. Wilde, U. Wallrabe, *J. Micromech. Microeng.* **2008**, *18*, 065008.

[22] S. Chen, B. Zhuo, X. Guo, *ACS Appl. Mater. Interfaces* **2016**, *8*, 20364.

[23] J. Park, Y. Lee, J. Hong, M. Ha, Y.-D. Jung, H. Lim, S. Y. Kim, H. Ko, *ACS Nano* **2014**, *8*, 4689.

[24] G. Y. Bae, S. W. Pak, D. Kim, G. Lee, D. H. Kim, Y. Chung, K. Cho, *Adv. Mater.* **2016**, *28*, 5300.

[25] B. Zhu, Z. Niu, H. Wang, W. R. Leow, H. Wang, Y. Li, L. Zheng, J. Wei, F. Huo, X. Chen, *Small* **2014**, *10*, 3625.

[26] J. Park, Y. Lee, S. Lim, Y. Lee, Y. Jung, H. Lim, H. Ko, *BioNanoScience* **2014**, *4*, 349.

[27] C. Pang, G.-Y. Lee, T.-i. Kim, S. M. Kim, H. N. Kim, S.-H. Ahn, K.-Y. Suh, *Nat. Mater.* **2012**, *11*, 795.

[28] H. Park, Y. R. Jeong, J. Yun, S. Y. Hong, S. Jin, S.-J. Lee, G. Zi, J. S. Ha, *ACS Nano* **2015**, *9*, 9974.

[29] M. Ha, S. Lim, J. Park, D. S. Um, Y. Lee, H. Ko, *Adv. Funct. Mater.* **2015**, *25*, 2841.

[30] S. Park, H. Kim, M. Vosgueritchian, S. Cheon, H. Kim, J. H. Koo, T. R. Kim, S. Lee, G. Schwartz, H. Chang, Z. Bao, *Adv. Mater.* **2014**, *26*, 7324.

[31] Z. He, W. Chen, B. Liang, C. Liu, L. Yang, D. Lu, Z. Mo, H. Zhu, Z. Tang, X. Gui, *ACS Appl. Mater. Interfaces* **2018**, *10*, 12816.

[32] W. Zhong, Q. Liu, Y. Wu, Y. Wang, X. Qing, M. Li, K. Liu, W. Wang, D. Wang, *Nanoscale* **2016**, *8*, 12105.

[33] Z. Chen, R. Ye, W. Lee, D. Jin, Y. Zhang, L. Jiang, Y. Yang, L. Ren, L. Jiang, *Adv. Electron. Mater.* **2019**, *5*, 1800785.

[34] Z. Chen, L. Ren, J. Li, L. Yao, Y. Chen, B. Liu, L. Jiang, *Acta Biomater.* **2018**, *65*, 283.

[35] J. V. Timonen, M. Latikka, L. Leibler, R. H. Ras, O. Ikkala, *Science* **2013**, *341*, 253.

[36] C. Pan, K. Chen, L. Jiang, Z. Chen, L. Ren, L. Liang, W. Yuan, *J. Mater. Process. Technol.* **2016**, *227*, 251.

[37] Y. Pang, K. Zhang, Z. Yang, S. Jiang, Z. Ju, Y. Li, X. Wang, D. Wang, M. Jian, Y. Zhang, R. Liang, H. Tian, Y. Yang, T.-L. Ren, *ACS Nano* **2018**, *12*, 2346.

[38] J. Lee, H. Kwon, J. Seo, S. Shin, J. H. Koo, C. Pang, S. Son, J. H. Kim, Y. H. Jang, D. E. Kim, Y. H. Jang, D. E. Kim, T. Lee, *Adv. Mater.* **2015**, *27*, 2433.

[39] C. Pang, J. H. Koo, A. Nguyen, J. M. Caves, M. G. Kim, A. Chortos, K. Kim, P. J. Wang, J. B. Tok, Z. Bao, *Adv. Mater.* **2015**, *27*, 634.

[40] J. Kim, T. N. Ng, W. S. Kim, *Appl. Phys. Lett.* **2012**, *101*, 103308.

[41] J. Yang, S. Luo, X. Zhou, J. Li, J. Fu, W. Yang, D. Wei, *ACS Appl. Mater. Interfaces* **2019**, *11*, 14997.

[42] J. Lee, H. Kwon, J. Seo, S. Shin, J. H. Koo, C. Pang, S. Son, J. H. Kim, Y. H. Jang, D. E. Kim, T. Lee, *Adv. Mater.* **2015**, *27*, 2433.

[43] X. Wei, L. Xiao, W. Huang, J. Liao, Z. D. Chen, *RSC Adv.* **2017**, *7*, 48354.

[44] S. Kang, J. Lee, S. Lee, S. Kim, J.-K. Kim, H. Algadi, S. Al-Sayari, D.-E. Kim, D. Kim, T. Lee, *Adv. Electron. Mater.* **2016**, *2*, 1600356.

[45] H. Kim, G. Kim, T. Kim, S. Lee, D. Kang, M. S. Hwang, Y. Chae, S. Kang, H. Lee, H. G. Park, W. Shim, *Small* **2018**, *14*, 1703432.

[46] J. C. Yang, J. O. Kim, J. Oh, S. Y. Kwon, J. Y. Sim, D. W. Kim, H. B. Choi, S. Park, *ACS Appl. Mater. Interfaces* **2019**, *11*, 19472.

[47] Y. Zhou, Y. Wu, W. Asghar, J. Ding, X. Su, S. Li, F. Li, Z. Yu, J. Shang, Y. Liu, R.-W. Li, *ACS Appl. Electron. Mater.* **2019**, *1*, 1866.

[48] K. Lee, J. Lee, G. Kim, Y. Kim, S. Kang, S. Cho, S. Kim, J. K. Kim, W. Lee, D. E. Kim, T. Lee, W. Shim, *Small* **2017**, *13*, 1700368.

[49] Z. Yu, J. Shang, X. Niu, Y. Liu, G. Liu, P. Dhanapal, Y. Zheng, H. Yang, Y. Wu, Y. Zhou, Y. Wang, D. Tang, R.-W. Li, *Adv. Electron. Mater.* **2018**, *4*, 1800137.

[50] S. Yao, Y. Zhu, *Nanoscale* **2014**, *6*, 2345.

[51] M. U. Khan, Z. Butt, H. Elahi, W. Asghar, Z. Abbas, M. Shoaib, M. A. Bashir, *Microsyst. Technol.* **2019**, *25*, 3235.

[52] S. Mukhtar, W. Asghar, Z. Butt, Z. Abbas, M. Ullah, R. Atta-Ur-Rehman, *J. Cent. South Univ.* **2018**, *25*, 2578.

[53] Y. Fan, C. Liao, L. Xie, X. Chen, *J. Mater. Chem. C* **2018**, *6*, 5401.

[54] Z. Liu, C. S. L. Chuah, M. G. Scanlon, *Acta Mater.* **2003**, *51*, 365.

[55] S. Böing, W. J. Randerath, *J. Thorac. Dis.* **2015**, *7*, 1273.

[56] R. Raphael, E. Dippenaar, *Int. Paramedic Pract.* **2019**, *9*, 41.

[57] C. Wilson, *J. Paramedic Pract.* **2018**, *10*, 370.

[58] A. Shepherd, S. C. Tsai, *Curr. Pulmonol. Rep.* **2017**, *6*, 82.

[59] A. J. Piper, B. J. Yee, *Compr. Physiol.* **2011**, *4*, 1639.

[60] M. G. Newman, H. Takei, P. R. Klokkevold, F. A. Carranza, *Elsevier Health Sci.* **2011**, *11*, 34.

[61] J. Ge, X. Wang, M. Drack, O. Volkov, M. Liang, G. S. C. Bermúdez, R. Illing, C. Wang, S. Zhou, J. Fassbender, M. Kaltenbrunner, D. Makarov, *Nat. Commun.* **2019**, *10*, 4405.